7-2013

Revision of empirical electric field modeling in the inner magnetosphere using Cluster data

Hiroshi Matsui
University of New Hampshire, matsui@spam.sr.unh.edu

Harlan E. Spence
University of New Hampshire, harlan.spence@unh.edu

Y. V. Khotyaintsev

P. A. Lindqvist

Revision of empirical electric field modeling in the inner magnetosphere using Cluster data

H. Matsui,[1] R. B. Torbert,[1] H. E. Spence,[1] Yu. V. Khotyaintsev,[2] and P.-A. Lindqvist[3]

[1]   Using Cluster data from the Electron Drift (EDI) and the Electric Field and Wave (EFW) instruments, we revise our empirically-based, inner-magnetospheric electric field (UNH-IMEF) model at $2 < L < 10$. We pick more EFW data during large activities when wake effects are expected to be small. The model is organized by either the interplanetary electric field (IEF) merging with the magnetosphere or the K_p index. IEF and K_p ranges for which we get potential patterns are, respectively: IEF<0.282 mV/m, 0.282<IEF<0.575 mV/m, 0.575<IEF<0.872 mV/m, 0.898<IEF<1.308 mV/m, 1.308<IEF<1.834 mV/m, 1.834<IEF<2.662 mV/m, and IEF>2.662 mV/m; $K_p < 1$, $1 \leq K_p < 2$, $2 \leq K_p < 3$, $3 \leq K_p < 4$, $4 \leq K_p < 5$, and $K_p \geq 4^+$. Patterns consist of one set of data and processing for smaller activities, and another for higher activities. As activity increases, the skewed potential contour related to the partial ring current appears on the nightside. With the revised analysis, we find that the skewed potential contours get clearer and potential contours get denser on the nightside and morningside. Since the fluctuating components are not negligible, standard deviations from the modeled values are included in the model. In this study, we perform validation of the derived model more extensively. We find experimentally that the skewed contours are located close to the last closed equipotential, consistent with previous theories. This gives physical context to our model and serves as one validation effort. As another validation effort, the derived results are compared with other models/measurements. From these comparisons, we conclude that our model has some clear advantages over the others.

1. Introduction

[2]   The electric field in the inner magnetosphere is related to transport of plasmaspheric and ring current particles [*Nishida*, 1966; *Kavanagh et al.*, 1968]. Formerly, ISEE 1, GEOS 2, and CRRES spacecraft measured such electric fields [*Maynard et al.*, 1983; *Baumjohann et al.*, 1985; *Rowland and Wygant*, 1998; *Wygant et al.*, 1998; *Rowland*, 2002]. In these studies, the measured electric fields showed dynamic behavior so that particle motions are expected to be complicated. This dynamic behavior was also reproduced by numerical simulations in which electric fields were self-consistently calculated [e.g., *Garner et al.*, 2004; *Liemohn et al.*, 2006].

[3]   These electric fields in the inner magnetosphere have been modeled for a long time based on various observations. One such model is the Volland-Stern model [*Volland*, 1973; *Stern*, 1975] in which electric potential patterns were obtained in the magnetic equator. *Maynard and Chen* [1975] determined the dependence of this model on the *Kp* index referring to the shape and the size of the plasmapause. *McIlwain* [1974, 1986] modeled the electric field referring to the measurement of injections of plasmasheet particles. In contrast to the equatorial electric field models noted above and others, there are a larger number of models at ionospheric heights. One such example often used in the community is the Weimer model [*Weimer*, 1995, 2001] based on electric field measurements made by the low-altitude satellite DE 2. In addition, there are various other models [*Foster*, 1986; *Rich and Maynard*, 1989; *Papitashvili et al.*, 1994; *Ruohoniemi and Greenwald*, 1996]. When we want to derive electric fields in the magnetosphere, these ionospheric values should be mapped adopting a magnetic field model such as the geomagnetic dipole field or the Tsyganenko model [*Tsyganenko*, 2002; *Tsyganenko and Sitnov*, 2005].

[4]   The Cluster spacecraft were launched in 2000 [*Escoubet et al.*, 2001]. Since then, the spacecraft are passing through the inner magnetosphere around their perigee in each polar orbit so that plenty of data are available.

[1]Space Science Center, University of New Hampshire, Durham, New Hampshire, USA.
[2]Swedish Institute of Space Physics, Uppsala, Sweden.
[3]Alfvén Laboratory, Royal Institute of Technology, Stockholm, Sweden.

Corresponding author: H. Matsui, Space Science Center, University of New Hampshire, 8 College Road, Durham, NH 03824, USA. (hiroshi.matsui@unh.edu)

There are two instruments onboard to measure electric fields: Electron Drift Instrument (EDI) [*Paschmann et al.*, 2001] and Electric Field and Wave (EFW) instrument *Gustafsson et al.*, [*Gustafsson et al.*, 2001]. These two instruments are complementary so that combination of both data enhances data availability. Using these data, we developed an empirically-based, inner magnetospheric electric field (UNH-IMEF) model in the equatorial plane [*Puhl-Quinn et al.*, 2008; *Matsui et al.*, 2008]. This model is useful for comparison with quantities derived from other measurements and/or simulations, such as locations of the inner edges of the electron plasmasheet and the plasmapause, electric fields themselves, etc.

[5] In order to develop the original model [*Matsui et al.*, 2008], we mainly used data from Cluster for > 5 years. The database was complemented by data from ground radars and an ionospheric spacecraft. Electric potential patterns were derived in the modeling domain which was $2 < L < 10$ and full magnetic local times (MLTs). The patterns were organized by the interplanetary electric field (IEF) affecting the magnetosphere. Key results on the derived potential patterns were as follows. As the IEF increases, the potential contours get denser. Equipotential contours on the nightside connecting the magnetotail and the near-Earth region are skewed toward the morningside, which is related to partial ring current [e.g., *C:son Brandt et al.*, 2002]. The original model was made open to public at http://edi.sr.unh.edu/unh-imef/.

[6] However, there is a problem in our previous work [*Matsui et al.*, 2008]. Data used to develop this model were mostly acquired during periods of quiet or moderate geomagnetic activities. We were not so sure about the behavior of electric fields during periods of high activity because of limited data coverage. Therefore, we proceeded to an analysis of electric fields during geomagnetic storm periods [*Matsui et al.*, 2010]. In that study, we analyzed Cluster electric field data for 71 storms during ∼7 years of operation. We introduced a scheme to include more EFW data than the one used in our previous modeling in order to achieve better data coverage. When we performed a superposed epoch analysis with an epoch at minimum *Dst* values of each storm, electric fields are enhanced around the epoch and decay in the recovery phase. We performed a similar superposed epoch analysis for IEF as well. Maximum IEF values cause minimum *Dst* values and maximum electric field values in the inner magnetosphere around the same time. The electric fields in the inner magnetosphere then decays on a similar time scale as the IEF, while *Dst* values recover on a longer time scale. Therefore, IEF could be a suitable parameter to organize the electric fields in the inner magnetosphere during storm periods.

[7] In the present study, we revise our electric field model based on the above previous work. We analyze more Cluster data. The procedure to incorporate electric field data into the database is evaluated in order to obtain optimal results. We check consistency between the model and theoretical expectations to get physical insights and thus to validate the model. Our results are compared with those from other models and measurements for further validation. This helps us highlight the specific merits of our model.

[8] Following this framework, the paper is organized as follows. In section 2, we describe our data analysis. We first review our previous analysis and then mention the revision introduced in this study. We also describe the specification of the new model. We generate a version organized by *Kp* index besides the one organized by the IEF and include standard deviations from the modeled values as well. In section 3, we show modeling results. Data distributions and derived potential patterns are presented. A physical implication of the skewed potential contours on the nightside is described. Variances of electric field values are derived. In section 4, we discuss our results, comparing with other models and measurements. Future possible work is briefly described. In section 5, conclusions are drawn.

2. Data Analysis

[9] In this section, we first summarize the data analysis performed in our previous study [*Matsui et al.*, 2008]. We then discuss the revision introduced in this study as well as the specification of the new model.

2.1. Previous Data Analysis

[10] In order to develop the original version of the model [*Matsui et al.*, 2008], we used electric field data measured by Cluster between February 2001 and October 2006. The EDI instrument measures two components of the electric fields perpendicular to the ambient magnetic field [*Paschmann et al.*, 2001]. Maximum time resolution of the data used in the analysis was 1 s. Although measured electric fields are generally reliable, there are data gaps especially during active periods and/or periods with large numbers of plasmasheet electrons [*Quinn et al.*, 2001]. The EDI emits artificial beams with energies of 500 eV and/or 1 keV from their electron guns and derive drift motions if beams return to the detectors. Tracking of the beams, and therefore acquisition of the data, becomes difficult if the geomagnetic conditions are active so that the electric and magnetic fields are variable. Another data loss occurs when the spacecraft is located in the plasmasheet. In this case, natural electrons tend to mask the electron beams. The EFW instrument measures two components of the electric fields in the spin plane of the spacecraft [*Gustafsson et al.*, 2001]. EFW data are continuously obtained. We used 4 s resolution data in Cluster Active Archive (CAA) [*Lindqvist et al.*, 2006; *Khotyaintsev et al.*, 2010]. In addition, the magnetic field data measured by the FluxGate Magnetometer (FGM) [*Balogh et al.*, 2001] were used during our data processing such as the conversion between the electric field and the convection velocity and the calculation of $E \cdot B = 0$. Time resolution of the data used in the analysis was 4 s. The Cluster's perigee was ∼4 R_E before 2006 so that we introduced data at $4 < L < 10$. Since the modeling domain was $2 < L < 10$, electric fields from ground radar measurements and ionospheric DE 2 measurements were introduced at $2 < L < 5$ based on published statistical results [*Blanc and Amayenc*, 1979; *Wand*, 1981; *Blanc*, 1983; *Ganguly et al.*, 1987; *Heelis and Coley*, 1992]. IEF merging with the magnetosphere measured by ACE [*Smith et al.*, 1998; *McComas et al.*, 1998] was an organizing parameter of our model. This value was defined as follows: IEF= $V\sqrt{B_Y^2 + B_Z^2}\sin^2(\theta/2)$, where V is the solar wind velocity, B_Y and B_Z are Y and Z components of the interplanetary magnetic field (IMF) in geocentric solar magnetospheric (GSM) coordinates, respectively, and θ is

the IMF clock angle. The clock angle is the polar angle in the GSM $Y-Z$ plane. Nominal propagation lags were compensated and 40 min averages were derived.

[11] EDI and EFW data were merged to create 4 s data in order to achieve maximum data availability [*Puhl-Quinn et al.*, 2008]. When EDI data were available, we used these data. Otherwise, EFW data were used, if the following two conditions were satisfied. (1) EFW data are overlapped with EDI data so that a median offset value can be determined in each 5 min interval. This offset value was subtracted from EFW data. (2) Also, the magnetic field direction must be >15° from the spacecraft spin plane. This condition was set because the non-spin-plane component of electric fields may well be estimated through the assumption of $\boldsymbol{E} \cdot \boldsymbol{B} = 0$. We set rather stringent conditions to introduce EFW data. This was because EFW data have artificial offsets from the actual values around perigee [*Puhl-Quinn et al.*, 2008]. The wakes due to the spacecraft motion relative to the ambient plasma were another cause for the offset [*Eriksson et al.*, 2006; *Engwall et al.*, 2009]. In addition, only two components of the electric field in the spin plane are measured by EFW as mentioned above.

[12] We derived electric potential patterns with these data sets following *Matsui et al.* [2004, 2008]. The merged electric field was averaged each 5 min. Then, the electric field values were mapped to the magnetic equator in solar magnetospheric (SM) coordinates using the *Tsyganenko* [2002] model. Further averages from 5 min values were calculated at each spatial bin ($\Delta L = 1$ and $\Delta MLT = 1$ h) and within each range of the organizing parameter, IEF. Our database has been divided to seven IEF ranges, in each of which we calculate a potential pattern. The numbers of 5 min data in each IEF range were not equally distributed. We allocated smaller numbers of data in larger IEF ranges so that average IEF values got larger in these IEF ranges. This was because we were often interested in potential patterns during active periods. These further averaged data in each bin were spatially interpolated up to two data points in the azimuthal direction or, in other words, 2 h in MLT, if there was a data gap. We then smoothed the data referring to the results at neighboring bins.

[13] In order to supplement Cluster data, ionospheric ground radar and DE 2 measurements were introduced at $2 < L < 5$. Ionospheric data were based on measurements at Millstone Hill [*Wand*, 1981], Saint-Santin [*Blanc and Amayenc*, 1979; *Blanc*, 1983], and Arecibo [*Ganguly et al.*, 1987]. Concerning DE 2 results, we took measurements of azimuthal ion drifts reported by *Heelis and Coley* [1992]. Since Cluster's perigee was ~4 R_E before 2006, it was possible to increase the spatial range of the modeling domain with these supplemental data. The results at $4 < L < 5$ were based on both Cluster data as well as these supplemental data. Next, potential patterns were calculated, which was considered as an inverse problem. The smoothness of the calculated potential patterns depends on the choice of a trade-off parameter, for which we followed the method taken by *Korth et al.* [2002]. Each calculated potential pattern was regarded as that corresponding to the average IEF value at each IEF range. A potential pattern at a specific IEF value was then interpolated or extrapolated from these potential patterns in seven IEF ranges.

2.2. Revised Data Analysis

[14] So far we have discussed our previous analysis. Here we update our analysis referring to our study on storm-time electric fields [*Matsui et al.*, 2010]. Below, we summarize that study. Since EDI data are often missing during active periods, the method to merge EDI and EFW data was revised. EFW data were included even if EDI data could not be compared with EFW data in each 5 min interval, when the spacecraft potential P measured by EFW was in a certain range: $-6 < P < -2$ V. The upper bound value was introduced to remove data with offsets between the two instruments reported by *Puhl-Quinn et al.* [2008]. The lower bound value was introduced in order to avoid data with wake effects reported by *Eriksson et al.* [2006] and *Engwall et al.* [2009]. A wake is a region downstream of a body where flow is disturbed because of the interaction between the flow and the body. An ion wake is formed behind a spacecraft when the bulk flow energy due to the plasma convection relative to the spacecraft is larger than the thermal energy. This causes a spurious electric field in the direction perpendicular to the real electric field. We introduced the above relaxation because we would otherwise have missed a large portion of data during the storm main phase. This is a period of interest to the space community as well as the subject of the study by *Matsui et al.* [2010]. The above relaxation is reasonable because this was based on the comparison between EDI and EFW data. In addition, nominal offsets have been subtracted from EFW data by the instrument team. Lastly, the main results of that study were in line with expectations from previous theories and observations. In *Matsui et al.* [2010], we only analyzed EFW data with good quality in the CAA database. Data with other qualities result from interferences from other instruments, wakes, etc. If we kept using such data, the possibility for obtaining meaningful results would be reduced.

[15] In this study, we revise our analysis in various aspects. First, we expand the database to include data until July 2010. The perigee of Cluster decreases after 2006 so that the Cluster data we analyze is $3 < L < 10$ instead of $4 < L < 10$ in the previous study [*Matsui et al.*, 2008]. Accordingly, we use ground radar and DE 2 results at $2 < L < 4$. EDI data with the ambiguity flag are not included in this study. The ambiguity flag is set when the measured electron motion during one cyclotron period includes large errors. Magnetic field data are now taken from CAA and those with caveats are removed. We then update our database. The revised merging of EDI and EFW data noted in the previous paragraph is introduced. As a result, more data during active periods are included. Simultaneously, we develop the database adopting the original merging scheme as well as the one only using EDI data. The calculated potential values from each scheme are compared in the next section.

[16] Interplanetary data analyzed in this study are OMNI data [*King and Papitashvili*, 2005] instead of ACE data we used before. The reasons are that multiple spacecraft data are incorporated into the OMNI data and that the time lag between the interplanetary spacecraft locations and the nose of the bow shock has already been corrected with a sophisticated method. Next, we select Cluster data inside the magnetosphere more carefully because the spacecraft may stay in the magnetosheath at $L < 10$ around the magnetic equator due to the modification of the Cluster's orbits
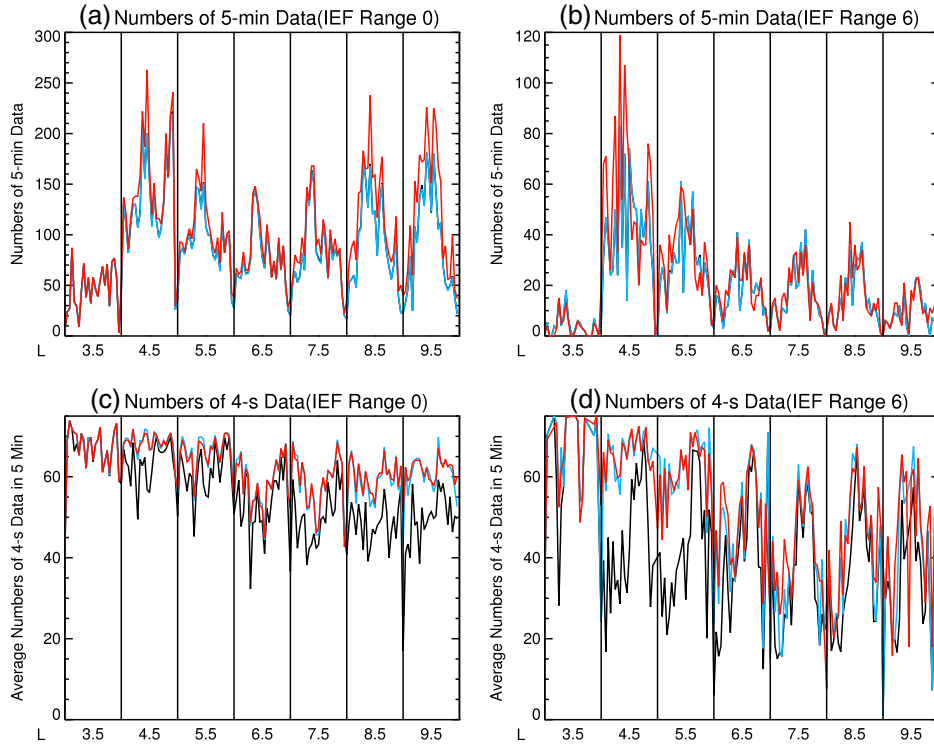
Figure 1. (a and b) Numbers of 5 min data points and (c and d) average numbers of 4 s data points in each 5 min interval. These values are shown for each spatial bin for two IEF ranges (Range 0 or the lowest IEF range in Figures 1a and 1c and Range 6 or the highest IEF range in Figures 1b and 1d). The horizontal axis shows spatial locations in the modeling domain. At each column of L shells, the results from 0.5 to 23.5 MLT are shown from left to right. Results for the following data-collecting schemes are shown: EDI data only (black), the original merging (blue), and the revised merging (red).

after 2006. Data obtained at radial distances < 2 R_E from or outside the expected magnetopause locations are not incorporated in our new database. Here a magnetopause model by *Shue et al.* [1998] is used. The choice of 2 R_E is the same as the criterion used by *Förster et al.* [2008]. In addition, the standard deviation of the modeled magnetopause locations in their former model [*Shue et al.*, 1997] is < 2 R_E. The mapping of the electric field from the spacecraft location to the magnetic equator along the magnetic field line is now performed using the model by *Tsyganenko and Sitnov* [2005] in which storm-time magnetic field is better reproduced than in previous Tsyganenko models [*Huang et al.*, 2008]. Interpolation of spatially averaged data is now performed up to three data points in the azimuthal direction. Further, we do not use the trade-off parameter prescribed by *Korth et al.* [2002] in order to derive the corotating potential because the corotating electric field is fairly stationary.

2.3. Specification of the Revised Model

[17] In the revised model, potential patterns are organized by both the IEF as well as the K_p index. The latter is newly introduced because of easier comparison with results from other studies [e.g., *Thomsen*, 2004] (see section 4). Although the time resolution (3 h) of this index is somewhat long, we still can resolve features longer than this. Such features have not been modeled using specifically measurements of the magnetospheric electric fields, as we do here. The number of IEF ranges to get each electric potential

pattern is seven, the same as the original model [*Matsui et al.*, 2008], while that of K_p ranges is six. The seven IEF ranges are as follows: IEF<0.282 mV/m, 0.282<IEF <0.575 mV/m, 0.575<IEF<0.872 mV/m, 0.898<IEF< 1.308 mV/m, 1.308<IEF<1.834 mV/m, 1.834<IEF< 2.662 mV/m, and IEF>2.662 mV/m. There is a small gap of the ranges at ∼0.9 mV/m because the exact boundary values depend on the data-merging. We have adopted two types of data-merging to derive final potential patterns, as discussed later. The six K_p ranges are as follows: K_p < 1, 1 ≤ K_p < 2, 2 ≤ K_p < 3, 3 ≤ K_p < 4, 4 ≤ K_p < 5, and K_p ≥ 4$^+$. The potential pattern at a specific IEF or K_p value is interpolated or extrapolated from the patterns originally derived in the above fixed IEF or K_p ranges referring to average IEF or K_p values in each range. Standard deviations from the modeled values are also included in the new model because of their potential relevance to the study of particle motion and stochastic acceleration, if any. Although the physics involved could be different, a similar approach was taken at thermospheric heights [*Deng et al.*, 2009]. The revised model is available at the same address as the original model: http://edi.sr.unh.edu/unh-imef/.

3. Modeling Results

[18] In this section, we first describe the data distribution in our database. This is followed by the selection of proper data-collecting schemes. Finally, the derived potential model is presented.
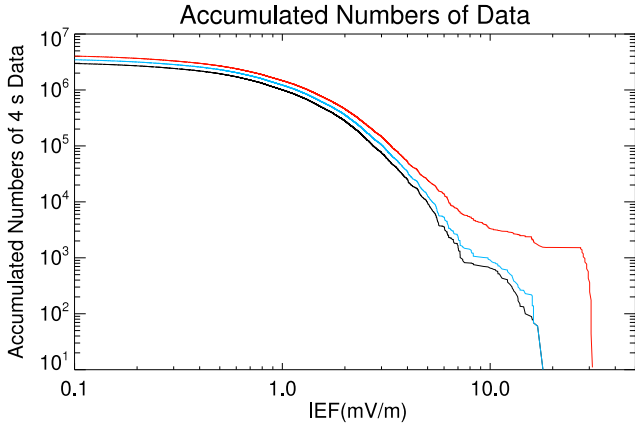
Figure 2. Distribution of IEF values in our database for three data-collecting schemes: EDI data only (black), the original merging (blue), and the revised merging (red). Accumulated numbers of 4 s data from the highest IEF values are plotted.

3.1. Data Distribution

[19] First, we describe the numbers of data points in each spatial bin for selected IEF ranges. Figure 1 shows numbers of 5 min data points (Figures 1a and 1b) and average numbers of 4 s data points in each 5 min interval (Figures 1c and 1d). Figures 1a and 1c show the numbers of data points in IEF Range 0 (the lowest IEF range), while Figures 1b and 1d show those in IEF Range 6 (the highest IEF range). The horizontal axis shows spatial locations in the modeling domain. At each column of L shells, the results from 0.5 to 23.5 MLT are shown from left to right. We have drawn the results for three data-collecting schemes in different colors: EDI data only (black), the original merging used in our previous modeling (blue), and the revised merging used in our storm analysis (red). In Figures 1a and 1b, there are fewer 5 min data at $L = 3.5$ than those at outer L shells because the smallest L value of each Cluster's orbit is ~ 4 before 2006. In Figures 1c and 1d, more 4 s data are available at low L shells because EDI tends to have a stable operation when the background magnetic field is large. In addition, there is an azimuthal asymmetry in the data distribution which can be seen as a variable number of data at each column of L shells. More 5 min data are available in the dayside MLTs, while more 4 s data are available in the eveningside and dayside MLTs. This is presumably due to the azimuthal asymmetries in the geomagnetic field, locations of the electron plasmasheet, etc. It should be noted that the occurrence distribution of 5 min averages does not have to be the same as that of average numbers of 4 s data points in each 5 min interval. Even if 4 s data are continuously obtained within each 5 min interval, the total number of 5 min intervals could be small. Such an example occurs when the time spent by spacecraft at each L shell is not equally distributed in the MLT direction due to the above-mentioned azimuthal asymmetries in the geomagnetic field. As more EFW data are introduced, the numbers of 5 min data points as well as average numbers of 4 s data points tend to increase. This can be seen by comparing data points in different colors. It should be noted that the numbers of 5 min data points are mostly overlapped between the database only using EDI data and

that using the original merging scheme, namely, that EFW data are included only when EDI data are available within 5 min. Therefore, the total number of 5 min data values does not increase from that when using only EDI data.

[20] Figure 2 shows distribution of IEF values in our database for three data-collecting schemes when electric field measurements are available. Accumulated numbers of 4 s data points counted from the highest IEF values are plotted. When EFW data are introduced as in the original merging, the number of data points increases in all IEF ranges compared to that of EDI data only. After the data-collecting scheme is revised from the original merging, we have more data especially during large IEF periods $> \sim 5$ mV/m.

3.2. Selection of Proper Electric Potential

[21] In this section, we compare electric potential values derived from three data-collecting schemes. Our concern is to judge which data-collecting scheme is most appropriate in order to derive potential patterns which are finally included in the model. With the revised merging, we have applied more data to the derivation of the model and so expect overall improvement, however, this is difficult to demonstrate directly owing to a paucity of independent correlative data and we instead argue for improvement based on evidence of greater physical realism and reduced contamination by instrumental effects. The physical significance is
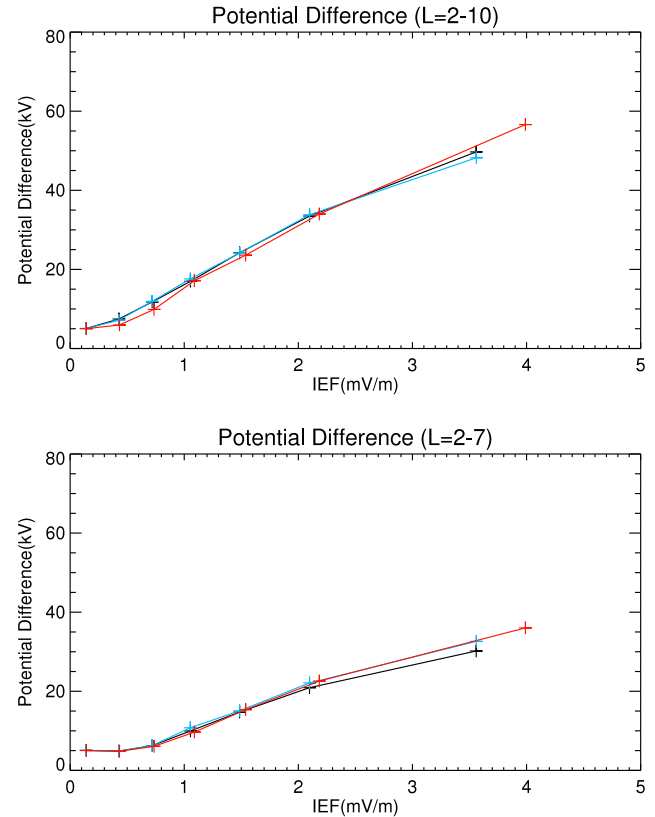

Figure 3. Electric potential differences between maximum and minimum values in two spatial domains at (top) $L = 2 - 10$ and at (bottom) $L = 2 - 7$. The results are plotted as a function of IEF for three data-collecting schemes. The meaning of each color is the same as in Figure 2.
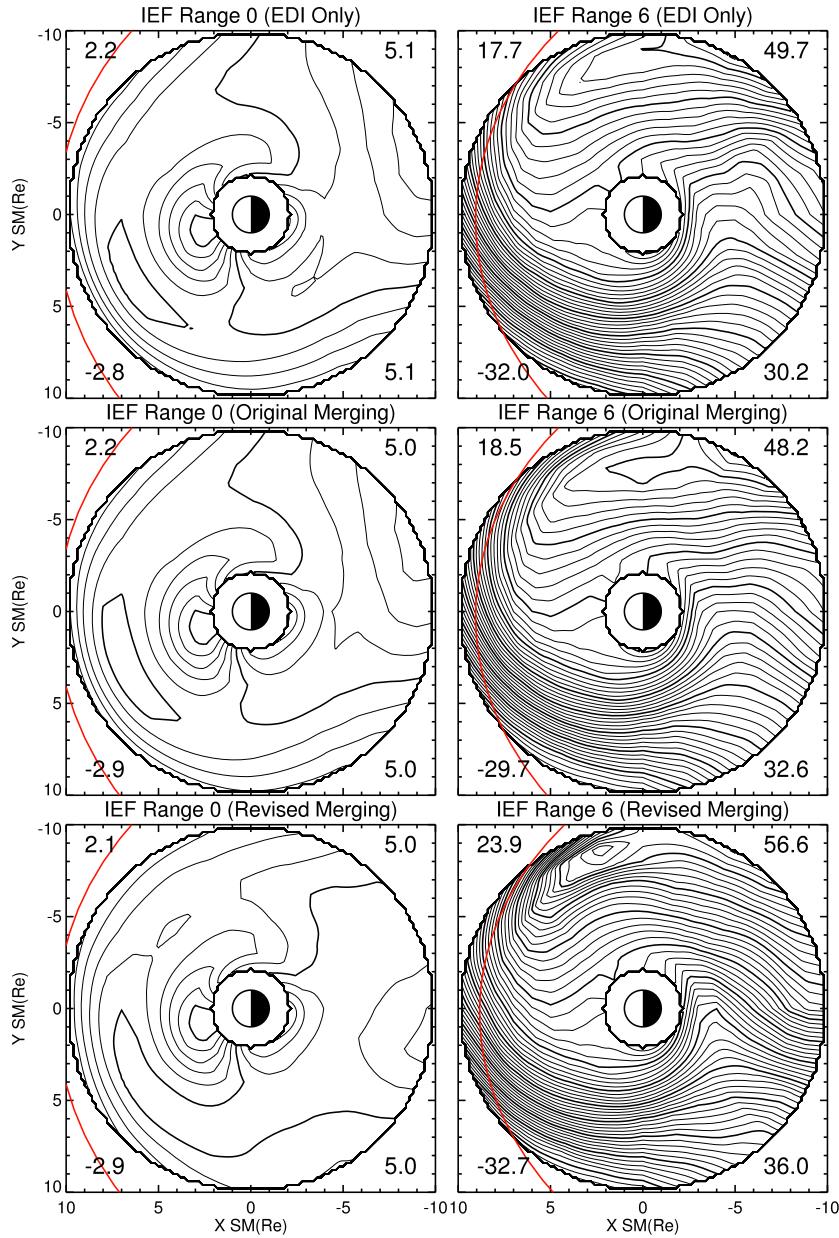
Figure 4. (left) Electric potential patterns for IEF Range 0 and for (right) IEF Range 6. The results for three data-collecting schemes are shown in the corotating frame. The contour intervals in Figure 4 (left) are 0.5 and 2.5 kV for thin and thick lines, respectively, while these are doubled in Figure 4 (Right). The numerical figures noted in each corner of the panels are maximum potential at $L = 2 - 10$ (Figure 4, top left), minimum potential at $L = 2 - 10$ (Figure 4, bottom left), potential difference at $L = 2 - 10$ (Figure 4, top right), and that at $L = 2 - 7$ (Figure 4, bottom right). The red line indicates expected locations of the magnetopause [*Shue et al.*, 1998].

checked for IEF dependence of the potential patterns as well as the skewed potential contours. The instrumental effect is checked in terms of the existence of the wake effects.

[22] First, we show the IEF dependence of the electric potential differences between maximum and minimum values in two spatial domains ($L = 2 - 10$ in Figure 3 (top) and $L = 2 - 7$ in Figure 3 (bottom)). The potential differences are plotted for three data-collecting schemes. Each data point corresponds to one of the seven IEF ranges in which we calculate a potential pattern. The average IEF value in the

largest IEF range in the revised merging is bigger than those in the other two schemes because we have managed to collect more data during large IEF periods. Potential differences are similar between various schemes except in the highest IEF range in both spatial domains.

[23] Next, we compare potential patterns from three data-collecting schemes (Figure 4). The patterns are depicted in the corotating frame. Figure 4 (left) shows patterns for IEF Range 0, while those for IEF Range 6 are depicted in the right three panels. The contour intervals for the left panels

are 0.5 and 2.5 kV for thin and thick lines, respectively, while these are doubled in the right panels. In each panel, overplotted in red are the modeled locations of the magnetopause after *Shue et al.* [1998]. We calculate these locations using average values of the input parameters to the model for the corresponding IEF range.

[24] First, we discuss the patterns in the lowest IEF range (left three panels). Overall, the potential patterns imply weak convection and are similar to each other. The comparison between the potential pattern with the revised merging and that with the more-selective, original merging indicates that the revised merging procedure sometimes includes points with wake effects, leading to spurious results (such as the orientation of the equipotentials in the dawn sector), so the original merging is to be preferred for this IEF range. It should be noted that we prefer to use the original merging scheme rather than the scheme only using EDI data because more data are included in the original merging with a conservative offset correction to EFW data.

[25] The right three panels show electric potential patterns for the IEF Range 6. These correspond to higher-convection patterns, where the revised merging yields a pattern similar to that for the other two data collecting schemes, but with better statistics. In addition, skewed contours on the nightside get clearer with the revised merging. Electric potential contours get denser on the nightside and on the morningside. The effect of the wake on the EFW measurement should decrease as IEF increases because the plasmasheet area gets wider. The occurrence condition of the wake, namely, that the bulk flow energy of the plasma is larger than its thermal energy, does not tend to be satisfied in the plasmasheet. This is the reason why the wake occurs more often during small IEF periods.

[26] As we have already seen, data included by relaxing the original merging criterion sometimes produce spurious features at low IEF ranges, probably because of the relatively larger number of wake-contaminated measurements under these low-IEF conditions. At high IEF ranges, wake contamination is less likely, and the derived patterns are similar to those of the other data collecting schemes, but they have better statistics, especially for stronger convection conditions, so the revised merging is preferable. The transition region of IEF, above which the revised merging is to be preferred is chosen to be IEF Range 3. The new model will be shown below to agree well with the other models and measurements. Therefore, we conclude that selectively increasing the data included in the model fits by slightly relaxing the selection criteria provides a better description of the average convection patterns in the magnetosphere at times of strong driving.

[27] After we revise the model, we include more data during large IEF periods than in the original model. When we compare the updated model with the original one (*Matsui et al.* [2008], Figure 4), the pattern in the largest IEF range has clearer skewed potential contours on the nightside. This is qualitatively consistent with the Rice Convection Model (RCM) simulated by *Garner et al.* [2004]. In addition, we have made an effort so that our data processing is more reasonable because we have taken into account characteristics of instruments more carefully. We also have introduced various procedures to validate the model. Therefore, we
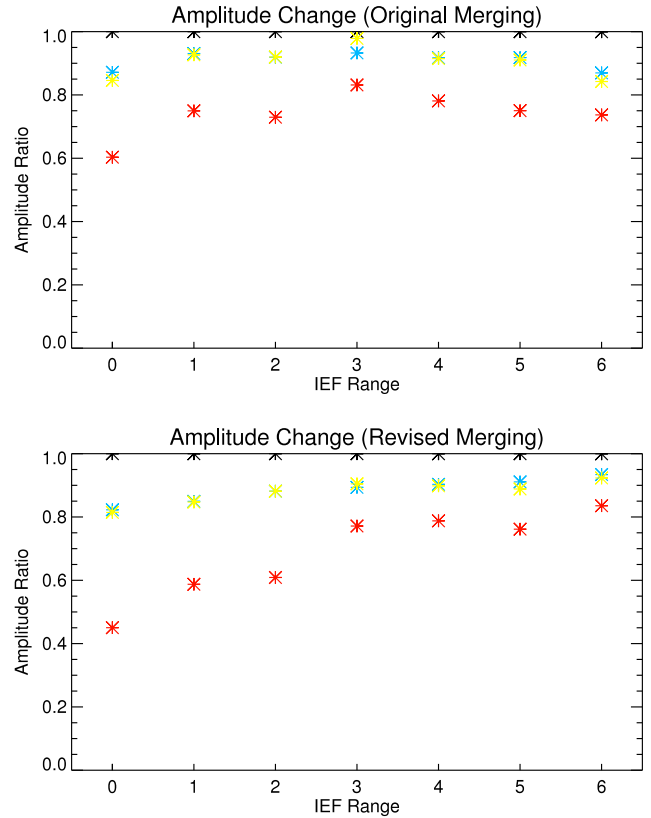

Figure 5. Amplitude change (see text) as a function of the IEF resulting from the data processing. Median values of the amplitude changes in the whole spatial bin at $L = 3 - 10$ are plotted for (top) the original merging and (bottom) the revised merging. Each color represents accumulated amplitude change from electric fields mapped to the magnetic equator and averaged at each spatial bin. The black points represent the amplitude change due to the neglect of the mapped E_Z components from the original values with three components. The blue points represent the amplitude change after the original values are smoothed. The yellow points represent the amplitude change after the ionospheric measurements are incorporated. Finally, the red points represent the amplitude change after potential patterns are derived.

expect that our model has been improved with respect to the previous one.

[28] Next, we show how the size of the electric field in our database is modified, and often reduced, during our data processing to derive potential patterns. Ideally, this size should be the same as that originally averaged at each spatial bin in the equator and at each IEF range. This is because the empirical model is supposed to reproduce this value. Therefore, we may consider the performance of the data processing to be better, the smaller such a modification of the size is. Here we evaluate this performance. Concerning the size of the electric field, we choose amplitude as a measure. The amplitude is calculated as the root of the sum of the squares of the three components of the electric field. Our calculation is performed in the corotating frame because we process data in this frame. Various procedures cause amplitude changes. These are calculated as the ratios of the amplitude at each stage of the data processing
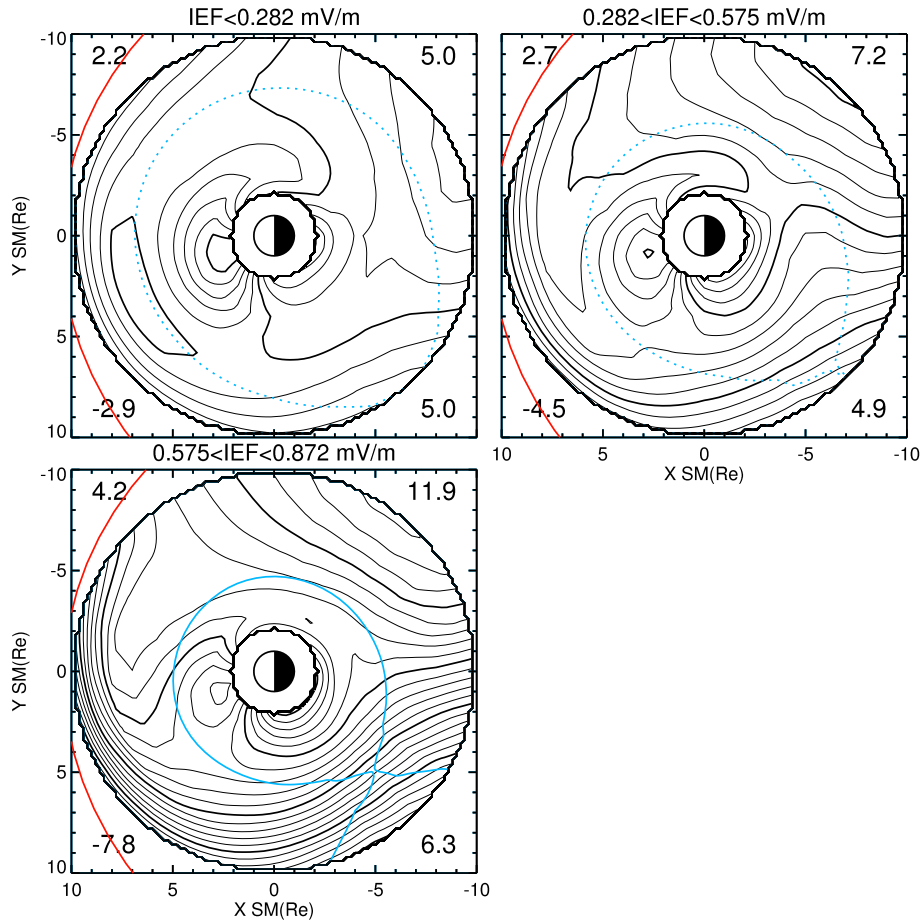
Figure 6. Electric potential patterns for three lower IEF ranges. Each panel is plotted in the corotating frame. The contour intervals are 0.5 and 2.5 kV for thin and thick lines, respectively. The solid, blue line indicates the potential contours near the last closed equipotential (LCE) calculated from our model in the inertial frame. The dotted, blue lines in the two lowest IEF ranges show the inner limit of the LCE because the stagnation point does not exist inside the modeling domain. The red lines indicate the modeled locations of the magnetopause. The numerical figures in each panel have the same meaning as those in Figure 4.

relative to the amplitude of the original field averaged at each spatial bin noted above. Median values of the ratios in the whole spatial bin at $L = 3 - 10$ are calculated for each IEF range and are plotted in Figure 5. Amplitude changes are derived after each of the following procedures: (1) neglect of mapped E_Z components (black points), (2) spatial smoothing (blue points), (3) incorporating supplemental ionospheric data (yellow points), and (4) fitting to potential patterns (red points). Concerning item 1, the electric field values mapped to the equator ($Z_{SM} = 0$) have Z components in SM coordinates because the magnetic field of the Tsyganenko model is not really parallel to the Z axis there. In our analysis, we neglect this E_Z component. The top and bottom panels in Figure 5 show the IEF dependence of the results for the original merging and the revised merging, respectively. When we inspect the figure, we find that the amplitude is mostly attenuated as the analysis proceeds. Items 2 and 4 contribute to the overall amplitude attenuation, while items 1 and 3 have marginal effects. The reason for the significant effect of item 2 is that the amount of data we analyze is limited. If our database is large enough, some of the spatial fluctuations in averaged values would be canceled out so that we do not

have to smooth our data. The reason for the significant effect of item 4 is that it is not always possible to integrate the electric fields into a potential form. The reason for the marginal effect of item 1 is that electric fields mapped to the magnetic equator generally have the Z components much smaller than the X or Y components. The reason of item 3 is that supplemental ionospheric data are only used around the lowest L value.

[29] Next, we compare the results for both merging schemes. The original merging leads to lower amplitude attenuation during small IEF periods, while the revised merging leads to lower attenuation during large IEF periods. Therefore, it makes sense to combine both merging schemes to get the final potential patterns. This is consistent with what we have already inferred while inspecting potential patterns for various data-collecting schemes. As noted, we have adopted the revised merging for the potential patterns above IEF Range 3 (IEF>0.898 mV/m). The amplitude attenuation plotted may support this choice, although it is hard to determine conclusively. When we calculate the median absolute deviation, this is always larger than the difference between the two merging methods.
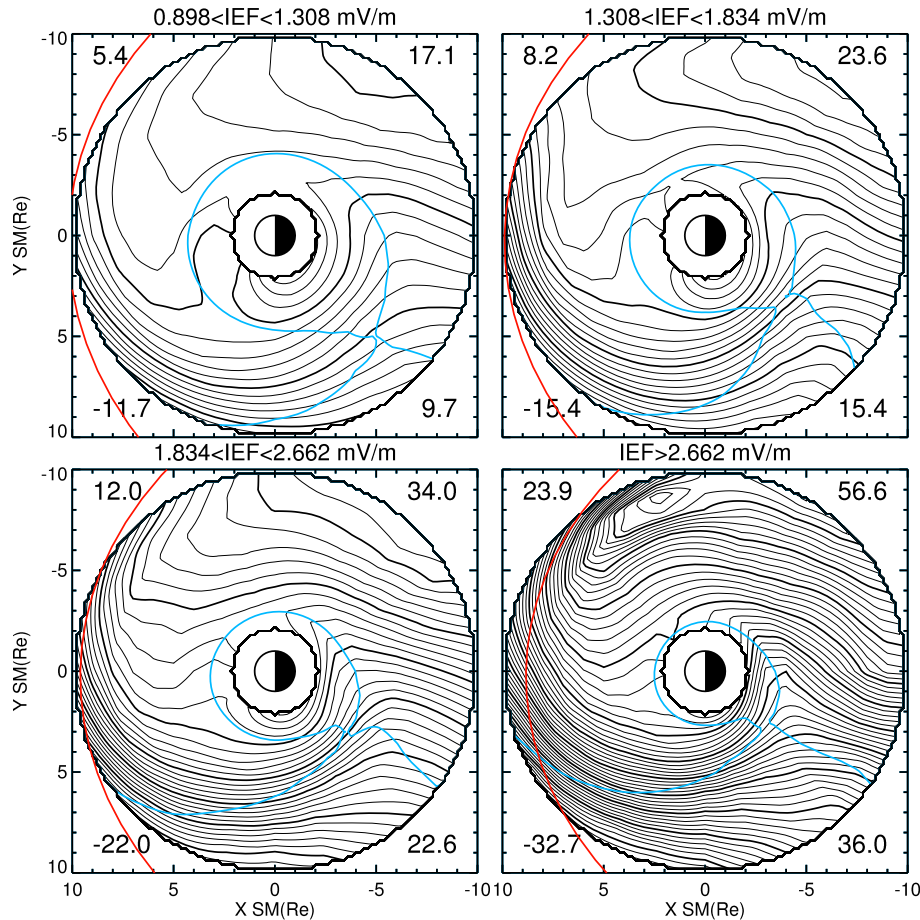
Figure 7. Electric potential patterns for four higher IEF ranges. Each panel is plotted in the corotating frame. The contour intervals are 1 and 5 kV for thin and thick lines, respectively. The meaning of lines and numerical figures in each panel is the same as that in Figure 6.

3.3. Derived Electric Potential

[30] Figure 6 shows potential patterns included in our new model made open to public for three lower IEF ranges, while Figure 7 shows those for four higher IEF ranges. The patterns for three lower IEF ranges are taken from the original merging, while those for four higher IEF ranges are taken from the revised merging. Contour intervals are 0.5 and 2.5 kV for thin and thick lines, respectively, in Figure 6, while those are doubled in Figure 7 in order to increase visibility. The solid, blue lines show the equipotential contours around the last closed equipotential (LCE) calculated from our model in the inertial frame. In order to calculate such contours, we first search for maximum potential in the radial direction at a fixed MLT value, and then get the minimum of these maximum potentials in the whole MLT range. Note that the calculated contour for the two lowest IEF ranges shown by dotted, blue lines are closer to the Earth than the actual LCE because the stagnation points do not exist inside the modeling domain. The red lines show the modeled locations of the magnetopause. When we compare potential patterns in both figures, there is a general dependence of the electric field strength on IEF as already inferred. When the IEF gets larger, skewed potential contours appear on the nightside. This skewed pattern tends to overlap the LCE. It is known that the direction of the potential contours skews

at the low latitude boundary of the auroral oval, where the ionospheric conductivity changes [*Vasyliunas*, 1970, 1972; *Senior and Blanc*, 1984]. This boundary is expected to be the ionospheric counterpart of the inner edge of the electron plasmasheet, which coincides with the LCE if the plasmasheet particles are continuously transported earthward up to the inner limit of accessible trajectories. The spatial variation of electric fields consistent with these skewed potential contours was also discussed by other authors [e.g., *Baumjohann*, 1983] as Harang discontinuity. *Gkioulidou et al.* [2009] examined formation of this discontinuity using the RCM. It should also be noted that the MLT of stagnation points shifts toward MLTs later than 18 MLT. This is consistent with the location of the plasmasphere bulge at that MLT [*Carpenter*, 1966; *Vasyliunas*, 1970]. However, this shift of the MLT looks inconsistent with *Korth et al.* [1999], where locations of plasmaspheric particles were well fitted to the Volland-Stern model with the stagnation point located at 18 MLT. There are two possible reasons for this inconsistency. The first is that the actual electric field may be different from that of the Volland-Stern model even though the LCE of the actual field is similar to that of the Volland-Stern model. This point is discussed in more detail in the next section. The second is that *Carpenter* [1966] chose steep density boundaries as the plasmapause, which may not include the plume
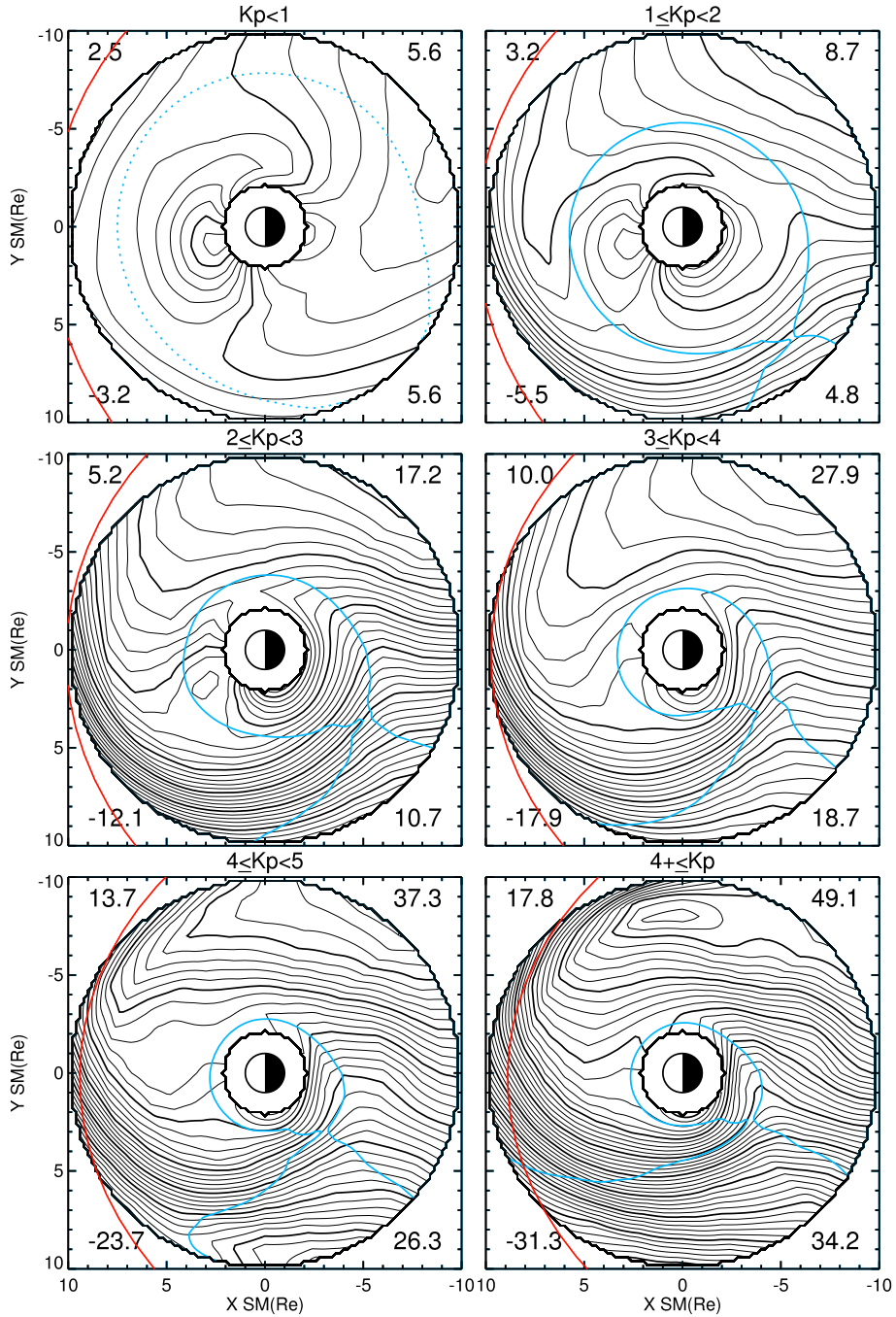
Figure 8. Electric potential patterns for six K_p ranges. Each panel is plotted in the corotating frame. The contour intervals are 0.5 and 2.5 kV for thin and thick lines, respectively, for the lower three K_p ranges, while those are doubled for the higher three K_p ranges. The meaning of lines and numerical figures in each panel is the same as that in Figure 6.

boundaries. Plumes are located outward of the plasmapause so that the density is more tenuous, which could make the density gradient less steep. Plume events were included in the study of *Korth et al.* [1999] together with the plasmaspheric bulge events. When we check our patterns against the modeled magnetopause locations, the modeling domain is partly situated outside for the largest IEF ranges. Even though each data point is $> 2\ R_E$ inside the expected magnetopause locations, it could be located outside the average locations for each IEF range.

[31] We also generate potential patterns organized by the K_p index (Figure 8). Here we divide data into six ranges. Patterns for the lower three K_p ranges are calculated with the original merging, while those for the higher three K_p ranges are calculated with the revised merging. The highest two K_p ranges are overlapped at $K_p = 4^+$ and 5^- in order to increase statistical significance. In the figure, the contour intervals for the lower three K_p ranges are half of the others. A dotted, blue line in the lowest K_p range shows the inner limit of the LCE because the potential contour near the LCE
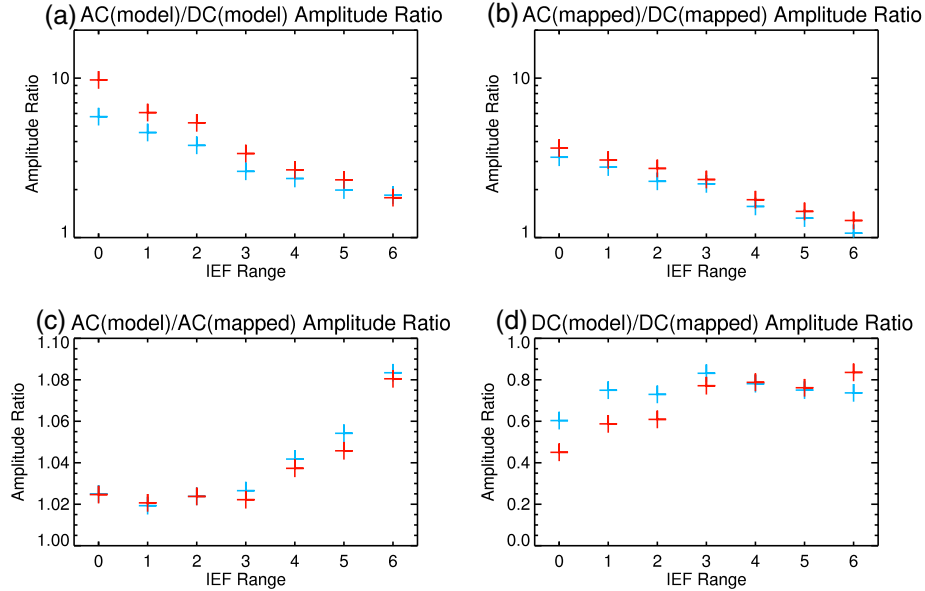
Figure 9. Amplitude ratios between the following quantities: modeled AC components, mapped AC components, modeled DC components, and mapped DC components. (For definition see text.) Each panel shows the following quantities: (a) the ratio of modeled AC components to modeled DC components, (b) the ratio of mapped AC components to mapped DC components, (c) the ratio of modeled AC components to mapped AC components, and (d) the ratio of modeled DC components to mapped DC components. Results for the original merging (blue) as well as the revised merging (red) are plotted in seven IEF ranges.

cannot be determined. When we inspect the figure, the general dependence of the patterns on the K_p index is similar to that on IEF.

[32] Next we compare (i) the electric fields mapped to the equator and averaged at each spatial bin, (ii) the modeled electric fields as derived above, and (iii) the fluctuating components of the electric fields (Figure 9). The two components in (i) and (ii) are referred to as mapped DC components and modeled DC components, respectively. Concerning fluctuating components (iii), we have derived variances of 5 min, mapped electric field values from their spatial averages and those from modeled values. These are referred to as mapped AC components and modeled AC components, respectively. These comparisons serve to evaluate the significance of the fluctuating components as well as the performance of the model. Modeled AC components are included in the model because these are often significant. In the figure, the amplitude ratios for the original and the revised merging are shown as a function of IEF by blue and red points, respectively. These ratios are calculated as median values of those in the whole spatial bin at $L = 3 - 10$, which is the same as Figure 5. In Figures 9a and 9b, AC components are larger than DC components, indicating that AC components are significant. This is especially true for the results in small IEF ranges consistent with *Matsui et al.* [2008]. Figures 9c and 9d show the ratio between modeled and mapped values for AC and DC components, respectively. The ratios for DC components have already been investigated in more details in Figure 5. When we compare the results for the original merging with those for the revised merging, the AC-AC ratios for the original merging are more different from 1 than those for the revised merging in larger IEF ranges (Figure 9c). Concerning this ratio, mapped AC components represent the naturally fluctuating components, while mod-

eled AC components include an offset due to the difference between modeled DC components and mapped DC components in addition to the naturally fluctuating components. Therefore, we expect that the ratio is close to one in an ideal case. The DC-DC ratios for the original merging are more different from 1 than those for the revised merging in smaller IEF ranges (Figure 9d). Concerning this ratio, we expect that the value is close to one in an ideal case as we have already discussed. This is because we are developing an empirical model, which should be similar to the observation. These two comparisons support the idea that the original merging is suitable in smaller IEF ranges, while the revised merging is suitable in larger IEF ranges.

4. Discussion

[33] In the above, we have derived potential patterns. We also have given a physical context to our model, which serves as a validation effort. In this section, we evaluate our results comparing with other models and measurements as another validation effort. We then suggest possible future validation of our model.

4.1. Comparison With Other Models and Measurements

[34] First, we calculate the electric potential differences between maximum and minimum values in two spatial domains ($L = 2 - 10$ and $2 - 7$) for various models: our model (black), Volland-Stern model with Maynard-Chen parameterization (yellow), the same model with Gussenhoven-Korth parameterization (red), and *Weimer* [2001] model (blue) (Figure 10). One thing to be careful about in this comparison is that each model is organized by different parameters. For example, the Volland-Stern model is organized
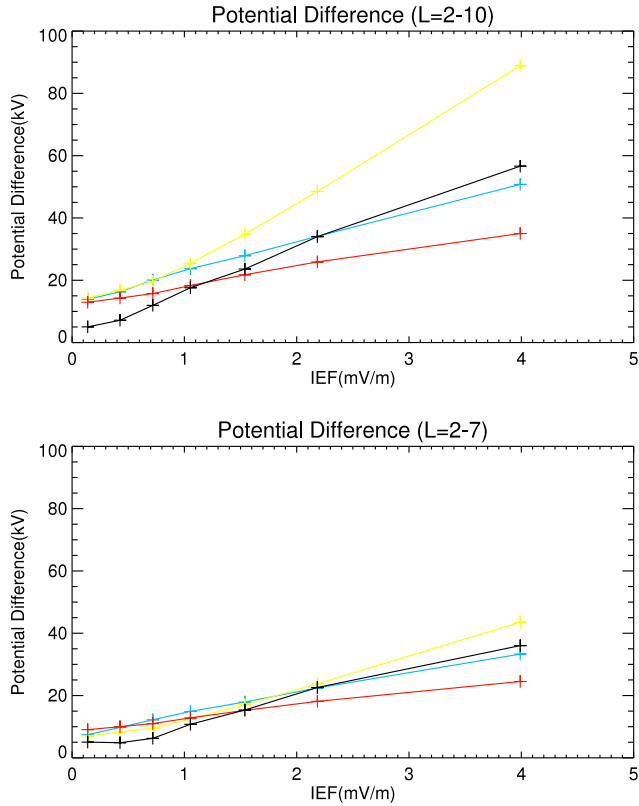
Figure 10. Electric potential differences between maximum and minimum values in two spatial domains at $L = 2 - 10$ (top) and at $L = 2 - 7$ (bottom) calculated as a function of IEF. The results of our model (black), Volland-Stern model with Maynard-Chen parameterization (yellow), the same model with Gussenhoven-Korth parameterization (red), and *Weimer* [2001] model (blue) are shown.

by the K_p index so that the average K_p value for each IEF range is calculated to drive that model. Note that *Matsui et al.* [2008] related K_p values to IEF values as performed here. This conversion could be one reason for the discrepancy between the results for each model. It should be noted that the Volland-Stern model has a flexibility regarding the magnitudes of electric fields and the shielding parameter, the latter of which is the exponent part of the base L in the potential form of the model. Here we choose two options. The first one refers to the parameterization given by *Maynard and Chen* [1975] with the shielding parameter 2. The second is taken from *Gussenhoven et al.* [1983]. One set of parameterization in their paper is consistent with the measurements of cold plasma at the geosynchronous orbit [*Korth et al.*, 1999]. The shielding parameter is 1, indicating there is no shielding. The results in Figure 10 are organized by the IEF in the same way as Figure 3. The difference in electrostatic potential predicted by each model and for each spatial domain increases as IEF increases. Despite this, the potential difference of the Volland-Stern model with Maynard-Chen parameterization tends to be larger than that of our model at $L = 2 - 10$ (top panel). In contrast, the potential difference of the Volland-Stern model with Gussenhoven-Korth parameterization tends to be smaller than that of our model at large IEF values. The potential differences predicted by

the Weimer model and our model are similar at large IEF values, but they are not at small IEF values. Potential differences for each model are generally similar at $L = 2 - 7$ (bottom panel), although our model again predicts smaller values than the other models in small IEF ranges.

[35] Next, we show potential contours around the LCE (Figure 11). Such potential contours are calculated using our model (solid, black), Volland-Stern model with Maynard-Chen parameterization (yellow), the same model with Gussenhoven-Korth parameterization (red), and *Weimer* [2001] model (blue). The results are organized by the K_p index, which is the same as in the Volland-Stern model. *Maynard and Chen* [1975] tried to match K_p-dependent locations of LCE in the Volland-Stern model with measured plasmapause locations. *Korth et al.* [1999] combined the Volland-Stern model with K_p-dependent locations of auroral boundaries derived by *Gussenhoven et al.* [1983] and confirmed that one of these combinations fits well with the cold plasma measurements at the geosynchronous orbit. The potential contours in the figure exactly match the LCE for the Volland-Stern model because the analytical derivation is possible. We cannot determine the contour near the LCE of our model for $K_p < 1$ which is the same as Figure 8. Therefore, the inner limit of the LCE is drawn by a dotted, black line. Since the Weimer model is organized by interplanetary parameters, we drive this model using interplanetary values in each K_p range. When we inspect the figure, the LCE of our model is located outward compared to that in the Volland-Stern model with both parameterizations in low K_p ranges. Since the size of the Volland-Stern model refers to the cold plasma location, the actual LCE could be located outward because enough quantities of plasmaspheric material may not exist up to the LCE. The LCE of the Weimer model is located inside those of the other models in low K_p ranges. In the intermediate K_p ranges, our model and the Volland-Stern model with Gussenhoven-Korth parameterization agrees best in the comparisons we made. This is true in all nightside MLTs, even though the plasmaspheric measurement was only performed at the geosynchronous orbit. The agreement between our model and that of Weimer improves as well. The agreement is not so good as the above between our model and that of Volland-Stern with Maynard-Chen parameterization. During large K_p periods, the LCE of our model is close to that of the Volland-Stern model with Gussenhoven-Korth parameterization between the premidnight and morning MLT sectors, while this is less so between the LCE of our model and those of the other models/parameterization. The LCE of our model does not agree with that of the Volland-Stern model with both parameterizations in the dusk sector. Note that the shape of the LCE of the Weimer model better agrees with that of our model for all $K_p \geq 2$, especially with respect to the MLT location of the stagnation point. In addition, the LCE of the Weimer model is similar to that of our model for the same K_p range except near midnight. The agreement is not so good when the LCE of the Volland-Stern model is compared to that in our model.

[36] Finally, Figure 12 shows comparison between CRRES measurements [*Rowland and Wygant*, 1998] and the following: (a) electric field from Cluster mapped to the equator, (b) our model, (c) Volland-Stern model with Maynard-Chen parameterization, (d) the same model with Gussenhoven-Korth parameterization, and
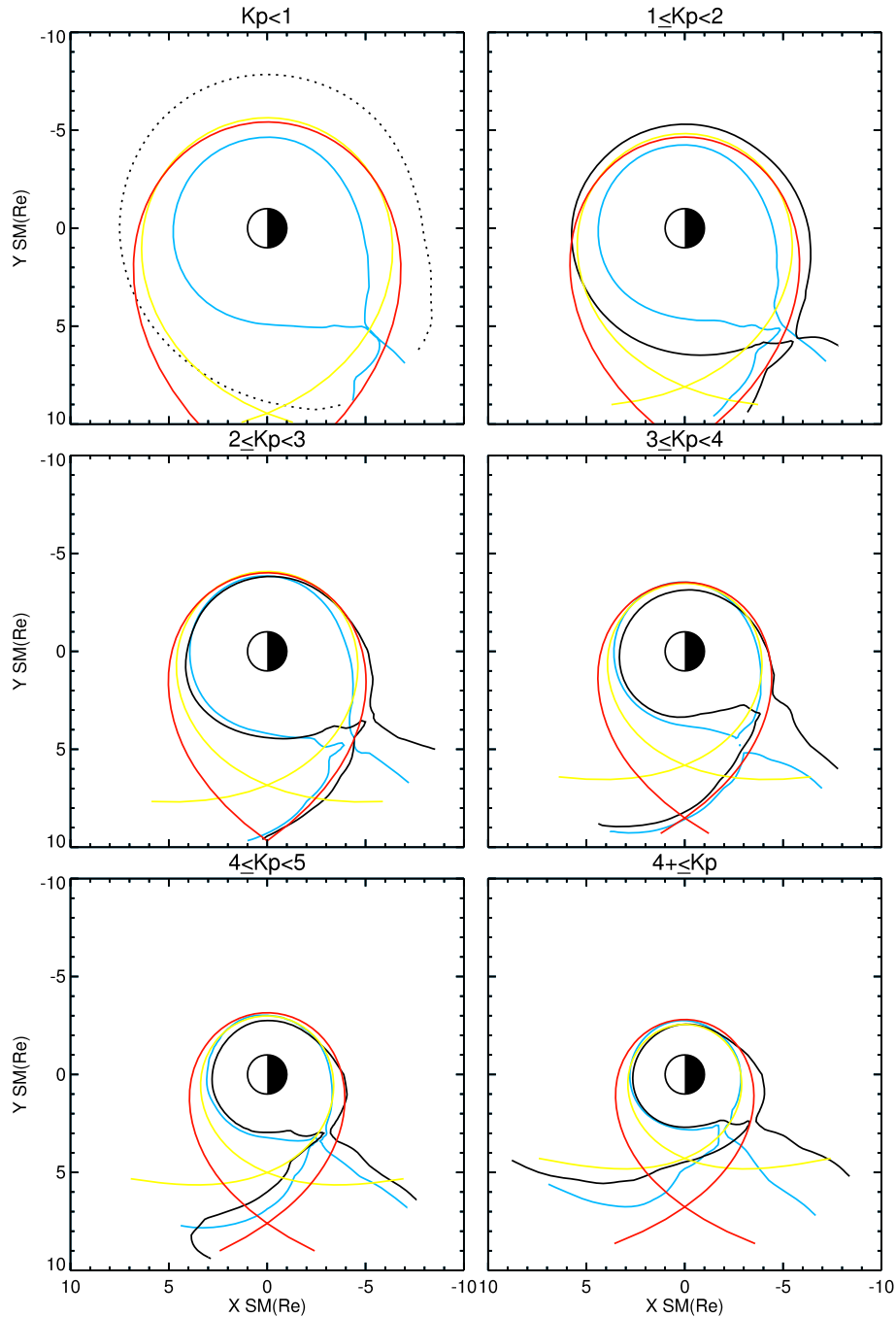
Figure 11. Potential contours around LCE of our model (solid, black), Volland-Stern model with Maynard-Chen parameterization (yellow), the same model with Gussenhoven-Korth parameterization (red), and *Weimer* [2001] model (blue) for various K_p ranges. Such a contour of our model cannot be determined at $K_p < 1$ so that the inner limit of the LCE is drawn by a dotted, black line.

(e) *Weimer* [2001] model. E_Y components at $12 - 04$ MLT are selected, which is the same as Plate 1 of *Rowland and Wygant* [1998]. The results are compared at various L values and K_p ranges indicated in the horizontal axis and by colors, respectively. CRRES results are shown by points, while other results are shown by lines. It should be noted that the highest K_p range in red is not exactly the same between these two, although there is an overlap (See the figure caption). In addition, we do not compare CRRES results at $K_p \geq 6$ with

the others because we did not calculate potential patterns limited to this K_p range. When we compare CRRES results with those from Cluster originally mapped to the equator, we find that they are similar in low and intermediate K_p ranges (Figure 12a). There is a tendency for the sign of dE_Y/dL to be positive for Cluster, although it is hard to see this in the highest K_p range because of fluctuations. The difference from CRRES measurements is $< \sim$ several tenths mV/m, which might be partly due to the different data coverage and
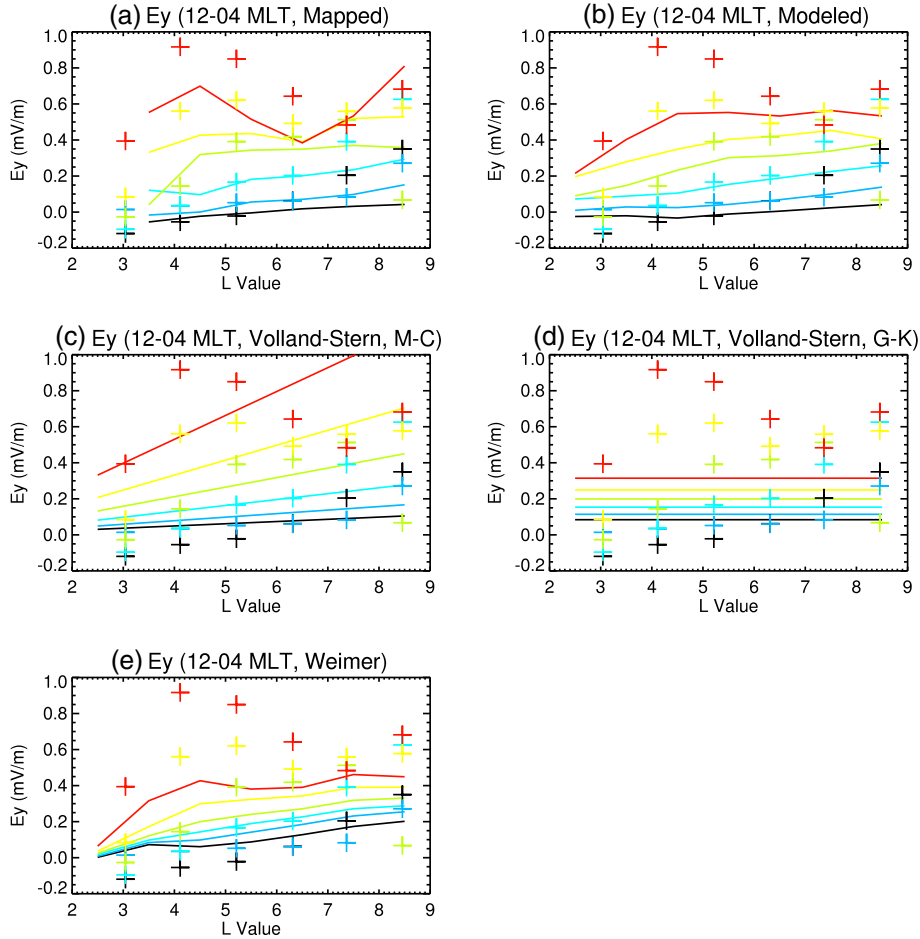
Figure 12. Comparison between CRRES measurements and the following measurements/models: (a) electric field from Cluster mapped to the equator, (b) our model, (c) Volland-Stern model with Maynard-Chen parameterization, (d) the same model with Gussenhoven-Korth parameterization, and (e) Weimer model. The E_Y values at $12 - 04$ MLT measured by CRRES are taken from *Rowland and Wygant* [1998]. CRRES results are shown by points, while other results are shown by lines. The meaning of each color for CRRES results is as follows: $K_p < 1$ (black), $1 \leq K_p < 2$ (blue), $2 \leq K_p < 3$ (light blue), $3 \leq K_p < 4$ (green), $4 \leq K_p < 5$ (yellow), and $5 \leq K_p < 6$ (red). The K_p ranges for the other results are the same as those for CRRES except at the highest range, where the K_p range for the other results is $4^+ \leq K_p$.

to the difference between mapped and in situ values. When we compare CRRES results with our modeled electric field in Figure 12b, the agreement is similar as in Figure 12a. In addition, the flat slope tends to show up for Cluster results in the highest K_p range possibly because of smoothing. In Figure 12c, the comparison between CRRES results and those from the Volland-Stern model with Maynard-Chen parameterization shows differences especially in the highest K_p range consistent with *Rowland* [2002]. The value of dE_Y/dL increases for this parameterization because of the shielding parameter independent of the K_p index. CRRES results are compared with the Volland-Stern model with Gussenhoven-Korth parameterization (Figure 12d). The results are not so similar to the CRRES measurements due to this particular parameterization without shielding. The electric fields derived from the Weimer model in Figure 12e tend to be smaller than those of CRRES during large K_p periods and to be larger during small K_p periods. This tendency is also true for the comparison between the Weimer model and our model.

[37] Thus far, we have compared our results with other models/measurements. We now summarize the results of these comparisons and discuss their implications. Concerning the Volland-Stern model with Maynard-Chen parameterization, the location of LCE is in fair agreement with that of our model. However, in the Volland-Stern model, the dependence of E_Y on the L value is not so realistic during large K_p periods. When we adopt instead Gussenhoven-Korth parameterization to the Volland-Stern model, the agreement of LCE with our model is the best. This is perhaps because their parameterization is based on an extensive statistical database from the Los Alamos National Laboratory (LANL) geosynchronous satellites. However, the dependence of E_Y on L value is not realistic because electric fields themselves are not compared between this model and the LANL data. Concerning the Weimer model, we find some agreements with our results. Although it is not easy to say which model is better, we point out that the Weimer model is based on the low-altitude measurements, while ours is based on the magnetospheric measurements. The location of LCE during

small K_p periods is more reasonable for our model because our LCE is located outward of the plasmaspheric material, while LCE of the Weimer model is located inward. Concerning the CRRES measurements, their reports are mainly limited to Y components, while ours is based on two perpendicular components. In summary, we believe that our model has some clear advantages over other models/measurements.

4.2. Future Validation Effort

[38] Another validation effort of our model would be to directly compare it with particle measurements. One such measurement is spatial distribution of particles at such locations as the inner edges of the electron plasmasheet, which are often used to estimate the electric field [e.g., *Gussenhoven et al.*, 1981; *Jiang et al.*, 2011]. Spatial distributions of the electron plasmasheet are frequently measured by Cluster EDI [*Quinn et al.*, 2001] and recently by the Van Allen Probes HOPE instrument [*Funsten et al.*, 2013]. This type of comparison will advance the understanding of the spatial relation between the skewed potential contour and the LCE. In addition, we expect to obtain further implications on the injection mechanisms of plasmasheet particles to the inner magnetosphere.

5. Conclusions

[39] We have been developing an empirically-based, inner-magnetospheric electric field (UNH-IMEF) model mainly using Cluster EDI and EFW data [*Puhl-Quinn et al.*, 2008; *Matsui et al.*, 2008]. Although the original model might be reasonable during quiet or moderate geomagnetic activities, this may not be so during high activities. We have therefore introduced more data during high activities. We have also added a longer period of data. In the revised model, the potential values are expressed as functions of either the IEF or the K_p index. When we inspect the derived potential patterns for small IEF periods, the original data-collecting scheme used by *Matsui et al.* [2008] seems to be reasonable. As the IEF increases, the potential difference in the modeling domain increases. We have shown experimentally that the skewed potential contours on the nightside are located close to the LCE, as predicted by previous theoretical work. This gives a physical context to our model and serves as one validation effort. We have managed to collect more data with the revised data-collecting scheme used by *Matsui et al.* [2010] than other schemes during large IEF periods. We have found that skewed potential contour gets clearer. The electric fields on the nightside and dawnside get larger. The dependence of the potential patterns on K_p index is similar to that on IEF. Despite these features, there is attenuation of electric field amplitude due to smoothing and fitting to the potential patterns when we process the data. As already discussed by *Matsui et al.* [2008], fluctuating electric fields are significant so that we include standard deviations from the modeled values. The revised model is available at the same address as the original model: http://edi.sr.unh.edu/unh-imef/.

[40] Our results are then compared with other models and measurements for further validation. There are some similarities between these, although there are discrepancies as well. Overall, the Volland-Stern model with Maynard-Chen parameterization has some similarities to our model regarding the LCE, although the shape of dE_Y/dL is not realistic during high K_p periods. Concerning the same model with Gussenhoven-Korth parameterization, the agreement of the locations of LCE with our model is the best of all the comparisons we have made, while the shape of dE_Y/dL is again not realistic. The Weimer model has some similarities to our model especially in the shape of the LCE in the stagnation regions, but they are based on the low-altitude data only. CRRES measurements are useful, but their investigations are mainly limited to E_Y components. Therefore, our model has some clear advantages over other models/measurements. We can further validate our model, e.g., by checking consistency between our model and spatial distribution of inner edges of the electron plasmasheet, which would be one possible future study using Van Allen Probes data.

References

Balogh, A., et al. (2001), The Cluster magnetic field investigation: Overview of in-flight performance and initial results, *Ann. Geophys.*, *19*, 1207–1217.

Baumjohann, W. (1983), Ionospheric and field-aligned current systems in the auroral zone: A concise review, *Adv. Space Res.*, *2*(10), 55–62.

Baumjohann, W., G. Haerendel, and F. Melzner (1985), Magnetospheric convection observed between 0600 and 2100 LT: Variations with Kp, *J. Geophys. Res.*, *103*, 393–398.

Blanc, M. (1983), Magnetospheric convection effects at mid-latitude 1. Saint-Santin observations, *J. Geophys. Res.*, *88*, 211–223.

Blanc, M., and P. Amayenc (1979), Seasonal variations of the ionospheric $E \times B$ drifts above Saint-Santin on quiet days, *J. Geophys. Res.*, *84*, 2691–2704.

Carpenter, D. L. (1966), Whistler studies of the plasmapause in the magnetosphere 1. Temporal variations in the position of the knee and some evidence on plasma motions near the knee, *J. Geophys. Res.*, *71*, 693–709.

C:son Brandt, P., S. Ohtani, D. G. Mitchell, M.-C. Fok, E. C. Roelof, and R. Demajistre (2002), Global ENA observations of the storm mainphase ring current: Implications for skewed electric fields in the inner magnetosphere, *Geophys. Res. Lett.*, *29*(20), 1954, doi:10.1029/2002GL015160.

Deng, Y., A. Maute, A. D. Richmond, and R. G. Roble (2009), Impact of electric field variability on Joule heating and thermospheric temperature and density, *Geophys. Res. Lett.*, *36*, L08105, doi:10.1029/2008GL036916.

Engwall, E., A. I. Eriksson, C. M. Cully, M. André, R. Torbert, and H. Vaith (2009), Earth's ionospheric outflow dominated by hidden cold plasma, *Nat. Geosci.*, *2*, 24–27.

Eriksson, A. I., et al. (2006), Electric field measurements on Cluster: Comparing the double-probe and electron drift techniques, *Ann. Geophys.*, *24*, 275–289.

Escoubet, C. P., M. Fehringer, and M. Goldstein (2001), The Cluster mission, *Ann. Geophys.*, *19*, 1197–1200.

Förster, M., S. E. Haaland, G. Paschmann, J. M. Quinn, R. B. Torbert, H. Vaith, and C. A. Kletzing (2008), High-latitude plasma convection during northward IMF as derived from in-situ magnetospheric cluster EDI measurements, *Ann. Geophys.*, *26*, 2685–2700.

Foster, J. C. (1986), Ionospheric convection associated with discrete levels of particle precipitation, *Geophys. Res. Lett.*, *13*, 656–659.

Funsten, H. O., et al. (2013), Helium, Oxygen, Proton, and Electron (HOPE) mass spectrometer for the radiation belt storm probes mission, *Space Sci. Rev.*, in press.

Ganguly, S., R. A. Behnke, and B. A. Emery (1987), Average electric field behavior in the ionosphere above Arecibo, *J. Geophys. Res.*, *92*, 1199–1210.

Garner, T. W., R. A. Wolf, R. W. Spiro, W. J. Burke, B. G. Fejer, S. Sazykin, J. L. Roeder, and M. R. Hairston (2004), Magnetospheric electric fields and plasma sheet injection to low L-shells during the 4–5 June 1991 magnetic storm: Comparison between the Rice convection model and observations, *J. Geophys. Res.*, *109*, A02214, doi:10.1029/2003JA010208.

Gkioulidou, M., C.-P. Wang, L. R. Lyons, and R. A. Wolf (2009), Formation of the Harang reversal and its dependence on plasma sheet conditions: Rice convection model simulations, *J. Geophys. Res.*, *114*, A07204, doi:10.1029/2008JA013955.

Gussenhoven, M. S., D. A. Hardy, and W. J. Burke (1981), DMSP/F2 electron observations of equatorward auroral boundaries and their relationship to magnetospheric electric fields, *J. Geophys. Res.*, *86*, 768–778.

Gussenhoven, M. S., D. A. Hardy, and N. Heinemann (1983), Systematics of the equatorward diffuse auroral boundary, *J. Geophys. Res.*, *88*, 5692–5708.

Gustafsson, G., et al. (2001), First results of electric field and density observations by Cluster EFW based on initial months of operation, *Ann. Geophys.*, *19*, 1219–1240.

Heelis, R. A., and W. R. Coley (1992), East-west ion drifts at mid-latitudes observed by dynamics explorer 2, *J. Geophys. Res.*, *97*, 19,461–19,469.

Huang, C.-L., H. E. Spence, H. J. Singer, and N. A. Tsyganenko (2008), A quantitative assessment of empirical magnetic field models at geosynchronous orbit during magnetic storms, *J. Geophys. Res.*, *113*, A04208, doi:10.1029/2007JA012623.

Jiang, F., M. G. Kivelson, R. J. Walker, K. K. Khurana, V. Angelopoulos, and T. Hsu (2011), A statistical study of the inner edge of the electron plasma sheet and the net convection potential as a function of geomagnetic activity, *J. Geophys. Res.*, *116*, A06215, doi:10.1029/2010JA016179.

Kavanagh, L. D., Jr., J. W. Freeman Jr., and A. J. Chen (1968), Plasma flow in the magnetosphere, *J. Geophys. Res.*, *73*, 5511–5519.

Khotyaintsev, Y., P.-A. Lindqvist, A. I. Eriksson, and M. André (2010), The EFW data in the CAA, in *The Cluster Active Archive, Studying the Earth's Space Plasma Environment*, edited by H. Laakso, M. G. T. T. Taylor, and C. P. Escoubet, pp. 97–108, Astrophysics and Space Science Proceedings, Springer, Berlin.

King, J. H., and N. E. Papitashvili (2005), Solar wind spatial scales in and comparisons of hourly wind and ace plasma and magnetic field data, *J. Geophys. Res.*, *110*, A02104, doi:10.1029/2004JA010649.

Korth, H., M. F. Thomsen, J. E. Borovsky, and D. J. McComas (1999), Plasma sheet access to geosynchronous orbit, *J. Geophys. Res.*, *104*, 25,047–25,061.

Korth, H., M. F. Thomsen, K.-H. Glassmeier, and W. S. Phillips (2002), Particle tomography of the inner magnetosphere, *J. Geophys. Res.*, *107*(A9), 1229, doi:10.1029/2001JA000147.

Liemohn, M. W., A. J. Ridley, J. U. Kozyra, D. L. Gallagher, M. F. Thomsen, M. G. Henderson, M. H. Denton, P. C. Brandt, and J. Goldstein (2006), Analyzing electric field morphology through data-model comparisons of the geospace environment modeling inner magnetosphere/storm assessment challenge events, *J. Geophys. Res.*, *111*, A11S11, doi:10.1029/2006JA011700.

Lindqvist, P.-A., Y. Khotyaintsev, M. André, and A. I. Eriksson (2006), EFW data in the cluster active archive, in *Proceedings Cluster and Double Star Symposium 5th Anniversary of Cluster in Space, Noordwijk, The Netherlands, 19 - 23 September 2005*, *Eur. Space Agency Spec. Publ., ESA SP-598*, p.68.1.

Matsui, H., V. K. Jordanova, J. M. Quinn, R. B. Torbert, and G. Paschmann (2004), Derivation of electric potential patterns in the inner magnetosphere from Cluster EDI data: Initial results, *J. Geophys. Res.*, *109*, A10202, doi:10.1029/2003JA010319.

Matsui, H., P. A. Puhl-Quinn, V. K. Jordanova, Y. Khotyaintsev, P.-A. Lindqvist, and R. B. Torbert (2008), Derivation of inner magnetospheric electric field (UNH-IMEF) model using Cluster data set, *Ann. Geophys.*, *26*, 2887–2898.

Matsui, H., P. A. Puhl-Quinn, J. W. Bonnell, C. J. Farrugia, V. K. Jordanova, Yu. V. Khotyaintsev, P.-A. Lindqvist, E. Georgescu, and R. B. Torbert (2010), Characteristics of storm time electric fields in the inner magnetosphere derived from cluster data, *J. Geophys. Res.*, *115*, A11215, doi:10.1029/2009JA015450.

Maynard, N. C., and A. J. Chen (1975), Isolated cold plasma regions: Observations and their relation to possible production mechanisms, *J. Geophys. Res.*, *80*, 1009–1013.

Maynard, N. C., T. L. Aggson, and J. P. Heppner (1983), The plasmaspheric electric field as measured by ISEE 1, *J. Geophys. Res.*, *88*, 3981–3990.

McComas, D. J., S. J. Bame, P. Baker, W. C. Feldman, J. L. Phillips, P. Riley, and J. W. Griffee (1998), Solar wind electron proton alpha monitor (SWEPAM) for the advanced composition explorer, *Space Sci. Rev.*, *86*, 563–612.

McIlwain, C. E. (1974), *Substorm injection boundaries*, in *Magnetospheric Physics*, edited by B. M. McCormac, 143–154, D. Reidel, Dordrecht, Netherlands.

McIlwain, C. E. (1986), A Kp dependent equatorial electric field model, *Adv. Space Res.*, *6*(3), 187–197.

Nishida, A. (1966), Formation of plasmapause, or magnetospheric plasma knee, by the combined action of magnetospheric convection and plasma escape from the tail, *J. Geophys. Res.*, *71*, 5669–5679.

Papitashvili, V. O., B. A. Belov, D. S. Faermark, Ya. I. Feldstein, S. A. Golyshev, L. I. Gromova, and A. E. Levitin (1994), Electric potential patterns in the northern and southern polar regions parameterized by the interplanetary magnetic field, *J. Geophys. Res.*, *99*, 13,251–13,262.

Paschmann, G., et al. (2001), The electron drift instrument on cluster: Overview of first results, *Ann. Geophys.*, *19*, 1273–1288.

Puhl-Quinn, P. A., H. Matsui, V. K. Jordanova, Y. Khotyaintsev, and P.-A. Lindqvist (2008), An effort to derive an empirically based, inner-magnetospheric electric field model: Merging cluster EDI and EFW data, *J. Atmos. Sol. Terr. Phys.*, *70*, 564–573.

Quinn, J. M., et al. (2001), Cluster EDI convection measurements across the high-latitude plasma sheet boundary at midnight, *Ann. Geophys.*, *19*, 1669–1681.

Rich, F. J., and N. C. Maynard (1989), Consequences of using simple analytical functions for the high-latitude convection electric field, *J. Geophys. Res.*, *94*, 3687–3701.

Rowland, D. E. (2002), The electrodynamics of the inner magnetosphere during major geomagnetic storms, PhD thesis, Univ. of Minn., Minneapolis.

Rowland, D. E., and J. R. Wygant (1998), Dependence of the large-scale, inner magnetospheric electric field on geomagnetic activity, *J. Geophys. Res.*, *103*, 14,959–14,964.

Ruohoniemi, J. M., and R. A. Greenwald (1996), Statistical patterns of high-latitude convection obtained from Goose Bay HF radar observations, *J. Geophys. Res.*, *101*, 21,743–21,763.

Senior, C., and M. Blanc (1984), On the control of magnetospheric convection by the spatial distribution of ionospheric conductivities, *J. Geophys. Res.*, *89*, 261–284.

Shue, J.-H., J. K. Chao, H. C. Fu, C. T. Russell, P. Song, K. K. Khurana, and H. J. Singer (1997), A new functional form to study the solar wind control of the magnetopause size and shape, *J. Geophys. Res.*, *102*, 9497–9511.

Shue, J.-H., et al. (1998), Magnetopause location under extreme solar wind conditions, *J. Geophys. Res.*, *103*, 17,691–17,700.

Smith, C. W., J. L'Heureux, N. F. Ness, M. H. Acuña, L. F. Burlaga, and J. Scheifele (1998), The ACE magnetic fields experiment, *Space Sci. Rev.*, *86*, 613–632.

Stern, D. P. (1975), The motion of a proton in the equatorial magnetosphere, *J. Geophys. Res.*, *80*, 595–599.

Thomsen, M. F. (2004), Why Kp is such a good measure of magnetospheric convection, *Space Weather*, *2*, S11004, doi:10.1029/2004SW000089.

Tsyganenko, N. A. (2002), A model of the near magnetosphere with a dawn dusk asymmetry 1. Mathematical structure, *J. Geophys. Res.*, *107*(A8), 1179, doi:10.1029/2001JA000219.

Tsyganenko, N. A., and M. I. Sitnov (2005), Modeling the dynamics of the inner magnetosphere during strong geomagnetic storms, *J. Geophys. Res.*, *110*, A03208, doi:10.1029/2004JA010798.

Vasyliunas, V. M. (1970), Mathematical models of magnetospheric convection and its coupling to the ionosphere, in *Particles and Fields in the Magnetosphere*, edited by B. M. McCormac, 60–71, D. Reidel, Dordrecht, Netherlands.

Vasyliunas, V. M. (1972), The interrelationship of magnetospheric processes, in *Earth's Magnetospheric Processes*, edited by B. M. McCormac, pp. 29–38, D. Reidel, Dordrecht, Netherlands.

Volland, H. (1973), A semiempirical model of large-scale magnetospheric electric fields, *J. Geophys. Res.*, *78*, 171–180.

Wand, R. H. (1981), A model representation of the ionospheric electric field over millstone hill ($\lambda = 56°$), *J. Geophys. Res.*, *86*, 5801–5808.

Weimer, D. R. (1995), Models of high-latitude electric potentials derived with a least error fit of spherical harmonic coefficients, *J. Geophys. Res.*, *100*, 19,595–19,607.

Weimer, D. R. (2001), An improved model of ionospheric electric potentials including substorm perturbations and applications to the Geospace Environment Modeling November 24, 1996, event, *J. Geophys. Res.*, *106*, 407–416.

Wygant, J., D. Rowland, H. J. Singer, M. Temerin, F. Mozer, and M. K. Hudson (1998), Experimental evidence on the role of the large spatial scale electric field in creating the ring current, *J. Geophys. Res.*, *103*, 29,527–29,544.